Accepted for publication in ApJ: July 15, 2011
Preprint typeset using LaTeX style emulateapj v. 04/20/08

RESOLVED SUBMILLIMETER OBSERVATIONS OF THE HR 8799 AND HD 107146 DEBRIS DISKS

A. Meredith Hughes[1,2], David J. Wilner[3], Sean M. Andrews[3], Jonathan P. Williams [4], Kate Y. L. Su[5], Ruth A. Murray-Clay[3], Chunhua Qi [3]

Accepted for publication in ApJ: July 15, 2011

ABSTRACT

We present 880 μm Submillimeter Array observations of the debris disks around the young solar analogue HD 107146 and the multiple-planet host star HR 8799, at an angular resolution of 3" and 6", respectively. We spatially resolve the inner edge of the disk around HR 8799 for the first time. While the data are not sensitive enough (with rms noise of 1 mJy) to constrain the system geometry, we demonstrate that a model by Su et al. (2009) based on the spectral energy distribution (SED) with an inner radius of 150 AU predicts well the spatially resolved data. Furthermore, by modeling simultaneously the SED and visibilities, we demonstrate that the dust is distributed in a broad (of order 100 AU) annulus rather than a narrow ring. We also model the observed SED and visibilities for the HD 107146 debris disk and generate a model of the dust emission that extends in a broad band between 50 and 170 AU from the star. We perform an *a posteriori* comparison with existing 1.3 mm CARMA observations and demonstrate that a smooth, axisymmetric model reproduces well all of the available millimeter-wavelength data.

Subject headings: circumstellar matter — planetary systems: debris disks — stars: individual (HR 8799, HD 107146)

1. INTRODUCTION

The tenuous, dusty debris disks orbiting main sequence stars are an important tracer of planetary system architectures and their dynamical evolution. With typical ages of 10-100 Myr, debris disks are analogous to our own solar system during the period when giant and terrestrial planets were undergoing heavy bombardment by small bodies. By this age, nearly all the primordial molecular gas has been dispersed from the protoplanetary disk, leaving a population of dust grains that should be removed by stellar radiation pressure on timescales much shorter than the age of the star. The dust is therefore thought to be generated by the grinding together of planetesimals that formed from the primordial disk material. Approximately 20% of nearby main sequence stars exhibit detectable infrared excesses indicative of debris disks, implying that planet formation at least to the stage of planetesimal growth is a common process (e.g., Habing et al. 2001; Carpenter et al. 2005; Bryden et al. 2006; Moór et al. 2010; Matthews et al. submitted). However, despite their prevalence in the solar neighborhood, the relatively faint emission from orbiting dust grains makes imaging challenging, and only a handful of systems have thus far been spatially resolved.

Observations at millimeter wavelengths have proven particularly valuable for studies of system dynamics, as these longer wavelengths are most sensitive to larger dust grains with long resonant lifetimes that trace best the structure resulting from orbital resonances (Wyatt 2006). To date, there have been only three debris disks spatially resolved with interferometers: β Pictoris, HD 107146, and HD 32297 (Wilner et al. 2010; Corder et al. 2009; Maness et al. 2008). In order to better understand the dust distribution in these systems and contribute to the sample of spatially resolved debris disk systems, we have observed two nearby, relatively bright debris disks with the Submillimeter Array (SMA), adding a new wavelength to the suite of observations of HD 107146 and spatially resolving the disk around HR 8799 for the first time.

HD 107146 is a rare example of a young, nearby, close solar analogue, with spectral type G2V (Jaschek 1978) and a distance of only 28.5 pc from the Sun (Perryman et al. 1997). Its age is estimated to lie between 80 and 200 Myr, although its location on the H-R diagram allows for an age as young as 30 Myr (Williams et al. 2004). It was identified as an "excess dwarf" on the basis of its *IRAS* colors by Silverstone (2000) and its debris disk was detected and marginally resolved for the first time at a wavelength of 450 μm by Williams et al. (2004). It has since been spatially resolved in near-infrared scattered light (Ardila et al. 2004; Ertel et al. 2011) as well as 350 μm, 1.3 mm and 3 mm dust continuum emission (Carpenter et al. 2005; Corder et al. 2009). Imaging reveals a broad debris belt with maximum brightness near a radius of $\sim$100 AU from the star, although detailed modeling of the millimeter data has not yet been carried out to determine its extent. Najita & Williams (2005) place an upper limit of 1 on the gas-to-dust mass ratio, indicating that the disk is largely devoid of primordial molecular gas. Corder et al. (2009) found that their 1.3 mm image exhibits possible azimuthal brightness asymmetries, and suggested the presence of a planet that is shepherding the material into resonances. Further observations of the large dust grain population are necessary to investigate that assertion.

[1] Department of Astronomy, University of California, Berkeley, 94720; mhughes@astro.berkeley.edu
[2] Miller Fellow
[3] Harvard-Smithsonian Center for Astrophysics, 60 Garden Street, Cambridge, MA 02138
[4] Institute for Astronomy, University of Hawaii, 2680 Woodlawn Dr., Honolulu, HI 96822
[5] Steward Observatory, University of Arizona, 933 N Cherry Avenue, Tucson, AZ 85721

HR 8799 is so far the only star to host a directly-imaged multiple-planet system. Four planets have been observed with projected orbital radii ranging from ∼15-80 AU (Marois et al. 2008, 2010). HR 8799 also hosts a debris disk, and was one of the twelve originally identified "Vega-like" stars based on its 60 μm *IRAS* flux (Sadakane & Nishida 1986). SED modeling suggests that there are at least two dust belts in the system, likely bracketing the radii of the innermost and outermost planets known: the inner belt has a temperature of ∼150 K and the outer belt has a temperature of ∼45 K (Williams & Andrews 2006; Chen et al. 2009; Su et al. 2009). Like all isolated young A stars (spectral type AV5, see e.g. Gray & Kaye 1999), its age is extremely difficult to determine, which is unfortunate because the masses of its planetary companions are estimated from hot-start models that depend sensitively on the assumed time since formation. Marois et al. (2008) estimate an age between 30 and 160 Myr based on several different indicators, which implies planet-mass companions (see also discussion in Hinz et al. 2010). Moya et al. (2010) favor an age as old as 1 Gyr based on an asteroseismological analysis, which would imply that the companions are in fact brown dwarfs, alothough an infrared color analysis by Currie et al. (2011) argues against such a high mass for the companions. The presence of a molecular gas filament coincident in space and recession velocity with HR 8799 (Williams & Andrews 2006; Su et al. 2009) may also point to a younger age. Spatially resolving the disk is therefore crucial, because it can provide new constraints on the companion masses. Both the age determination and the stability of the planetary system depend sensitively on the unknown viewing geometry (Fabrycky & Murray-Clay 2010), which can be determined by spatially resolved observations of the disk, assuming coplanarity. Spatially resolving the dust distribution, particularly at long wavelengths, also places a more direct dynamical constraint on the mass of the outermost planet independent of the age of the system (see, e.g., Chiang et al. 2009).

To investigate the spatial distribution of large dust grains and their implications for inferring the presence and properties of planets in the systems, we observed HD 107146 and HR 8799 with the SMA at a frequency of 880 μm. The observations are described in Section 2 and the results are presented in Section 3. We generate a model of the disk around HD 107146 that is capable of reproducing both the SED and SMA visibilities and compare it with the previous 1.3 mm CARMA observations in Section 4.1. We perform a simplified analysis on the lower signal-to-noise HR 8799 data in Section 4.2, comparing the data with the SED-based model from Su et al. (2009) and investigating whether the data can distinguish between a broad and narrow dust ring. We discuss the implications of these results for the properties of the systems in Section 5, and summarize our conclusions in Section 6.

2. OBSERVATIONS

HR 8799 was observed during four nights in the fall of 2009. Basic observing parameters are listed in Table 1. Precipitable water vapor was very low on all three nights, with the 225 GHz opacity holding steady at around 0.06. Phase stability was more variable: September 20 had the best phase stability, while the second half of the night on October 1 was nearly unusable, exhibiting substantial phase decorrelation corresponding to large spikes in humidity measured at the summit of Mauna Kea. Observations of HR 8799 were interleaved with 3C454.3, one of the brightest quasars in the sky and only 6° away from the target, to calibrate the atmospheric and instrumental phase variations. The quasar J2232+117 was included in the observing loop to test the efficacy of the phase transfer. To emphasize the emission on the shortest baselines, we image the combined dataset with a 6" taper, resulting in an rms noise of 1.1 mJy beam^{-1}.

HD 107146 was observed during four nights in early 2009. Basic observing parameters are listed in Table 1. The weather was excellent on all nights, although the night of January 21 was particularly spectacular with a 225 GHz opacity dropping rapidly from 0.06 to 0.03, and remaining low throughout the night. Observations of HD 107146 were interleaved with the quasars 3C273 (15° away) and 3C274 (5° away) to calibrate the atmospheric and instrumental gains. Despite the presence of a bright, spatially extended jet observed at longer radio wavelengths (e.g. Owen et al. 1980), we detect extended structure around 3c274 at a level of only a few percent of the core flux, at a position angle coincident with the known jet location. The marginally resolved 3c274 structure had minimal effect on the resulting visibilities, with phase transfer to 3c273 resulting in point-like visibilities to within <0.″3. We image the combined dataset with a 1.″2 taper, resulting in an rms noise of 0.7 mJy beam^{-1}.

The local oscillator (LO) frequency was 341.493 GHz for the HR 8799 observations and 340.755 GHz for the HD 107146 observations. The full 8 GHz bandwidth (4 GHz in each sideband separated by ±5 GHz from the LO frequency) was sampled evenly at a relatively low spectral resolution of 0.7 km s^{-1} to maximize continuum sensitivity. Routine calibration tasks were carried out using the MIR[6] software package, while imaging and deconvolution were accomplished using the MIRIAD software package. To estimate the effects of phase instability on seeing, we fit Gaussian functions to the test quasars and measure sizes of 0.″1±0.″1 for 3C273 (HD 107146) and 0.″2±0.″3 for J2232+117 (HR 8799). The 3σ upper limits on the seeing are approximately an order of magnitude lower than the spatial resolution of the final images.

3. RESULTS

We detect 880 μm continuum emission from HD 107146 on all four nights; the combined map and visibilities are displayed in the left panels of Figure 1. The emission is distributed in a ring around the position of the star, which is adjusted for proper motion and marked with a star symbol in the figure. The peak brightness of the ring occurs at approximately 3.″5 from the star position, which corresponds to a linear separation of 100 AU at a distance of 28.5 pc. There is a deficit of emission coincident with the star position that suggests the presence of a central cavity in the dust distribution. Using the MIRIAD task `cgcurs`, we estimate an integrated flux density of 36±1 mJy.

Due to periods of atmospheric phase instability, large portions of the nights of September 20 and October 1 were unusable, resulting in an rms noise for each night

[6] See http://cfa-www.harvard.edu/∼cqi/mircook.html

TABLE 1
Basic Observing Parameters

Date	Baseline lengths (m)	225 GHz opacity	Flux calibrator	Derived gain cal flux[a] (Jy)
HR 8799				
Sep 20	9.5-68	0.06	Ganymede	16.1
Sep 21	9.5-68	0.06	Callisto	16.7
Oct 1	9.5-68	0.06	Callisto	19.9
HD 107146				
Jan 6	16-69	0.07	Titan	1.3
Jan 21	9.5-69	0.03-0.06	Titan	1.2
Feb 1	9.5-69	0.06	Ceres	1.1
May 2	25-139	0.05	Titan	1.1

[a]The quasars used as gain calibrators were 3C454.3 for HR 8799 and 3C274 for HD 107146.

that was approximately a factor of two larger than the rms noise on September 21. As a result, we detect emission from the HR 8799 disk only on the night of September 21. The left panel of Figure 2 displays the combined map and the right panel shows the visibilities. The peak signal-to-noise ratio is 4.3, and the emission peak occurs 5.5" from the star. There is some suggestion that the emission is slightly extended along an arc of the same radius, as would be expected if it were distributed in a ring around the star. It is impossible to determine from the images alone the underlying radial distribution of the dust grains or the degree of azimuthal (a)symmetry of the emission, due to the low signal-to-noise ratio and incomplete sampling of the (u,v) plane. In Section 4, we therefore model the underlying dust distribution to constrain its extent and to search for asymmetries in the residuals.

3.1. *Line-of-Sight CO Towards HR 8799*

We detect the CO(3-2) emission reported by Williams & Andrews (2006) and demonstrated by Su et al. (2009) to be at an LSR velocity coincident with that of HR 8799. The line emission is quite narrow, appearing in only two of the $0.7\,\mathrm{km\,s^{-1}}$ channels, indicating a linewidth of $\lesssim 1.4\,\mathrm{km\,s^{-1}}$. The line does not image cleanly in the interferometric data, exhibiting striping from northeast to southwest across the image. There are two likely reasons for this: (1) the position angle of the stripes matches that of the CO filament in Figure 4 of Williams & Andrews (2006), and the separation between stripes is equal to that between the peak of the synthesized beam and its largest (30%) sidelobes, and (2) there is a knot of bright CO emission visible in the JCMT map to the northwest of the SMA map center at a distance of approximately the width of the SMA primary beam, which coincides with a peak in the SMA map. Not only are interferometers inherently poorly suited to imaging extended emission like the CO filament observed with the JCMT, but the presence of a bright source outside the primary beam on its own would be expected to cause striping across the image. Nevertheless, there is no evidence of a velocity gradient across the line, which is characteristic of rotation and would be expected if the CO(3-2) emission were associated with the disk. Given the spatial resolution of the SMA, such a gradient should be easily detectable if it were present. Assuming a gas disk spatially coincident with the observed dust emission, the CO(3-2) line should be concentrated well within the 30" SMA primary beam and should exhibit centroid shifts across the line by ∼5" between the red and blue channels, which is not observed. We therefore conclude that the CO emission does not originate from the disk around HR 8799, although the coincidence in spatial location and velocity are suggestive that the disk may be associated with the CO filament.

4. ANALYSIS

In order to constrain the spatial distribution of circumstellar dust in these systems, we model simultaneously the spectral energy distribution (SED) and spatially resolved $880\,\mu$m visibilities. Section 4.1 describes the modeling procedure used for HD 107146, including an *a posteriori* comparison between the model of the SMA data and previous spatially resolved observations of HD 107146 with CARMA. Section 4.2 describes how we modify this procedure for the low signal-to-noise case of HR 8799.

4.1. *HD 107146 Modeling Procedure*

The bottom right panel of Figure 1 shows the HD 107146 SED assembled from the literature (Landolt 1983; Williams et al. 2004; Carpenter et al. 2005; Moór et al. 2006; Hillenbrand et al. 2008; Corder et al. 2009, plus IRAS and 2MASS fluxes). We model the SED with three components: (1) a Kurucz model stellar photosphere with surface gravity $\log g$=4.5 and effective temperature T_{eff}=5859 K (Carpenter et al. 2008; Hillenbrand et al. 2008); (2) a dust belt with a temperature of 69 K, which is required to reproduce the mid-IR fluxes but does not contribute substantially to the millimeter-wavelength flux; and (3) an outer debris belt with the properties described below. It is this latter component that accounts for effectively all of the $880\,\mu$m flux, and it must therefore be modeled as a spatially extended component to reproduce both the observed visibilities and the SED.

As in Williams et al. (2004), we assume a dust grain emission efficiency $Q_\lambda = 1 - \exp\left[-(\lambda_0/\lambda)^\beta\right]$, where λ_0 is a critical wavelength; this has the desired asymptotic behavior that $Q_\lambda = (\lambda_0/\lambda)^\beta$ for $\lambda >> \lambda_0$ and $Q_\lambda = 1$ for $\lambda << \lambda_0$, while varying smoothly between the two extremes. However, unlike Williams et al. (2004) who fit the SED with a single dust temperature, we require the dust grains to be in radiative equilibrium with the star and allow the disk to be spatially extended. With these assumptions, using the textbook formulation from

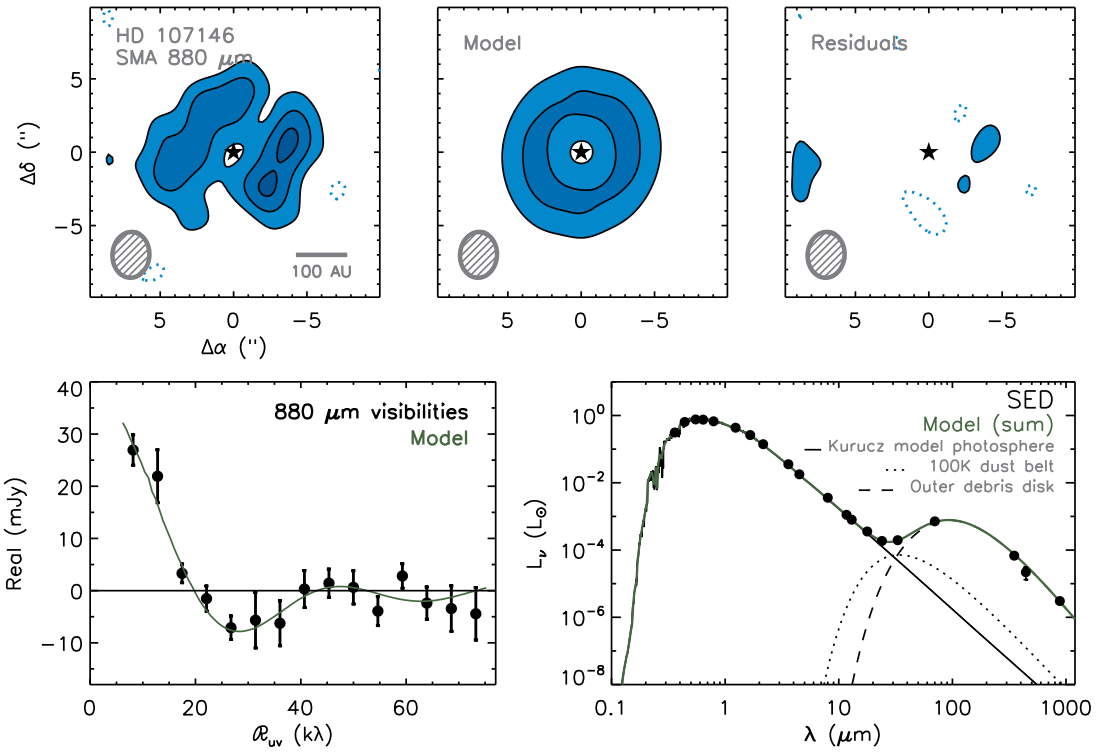

FIG. 1.— Comparison between HD 107146 data and the best-fit model for the SED and visibilities. The top row shows the SMA 880 μm data (left), model (center), and residuals (right) in the image domain, with contours [2,4,6]×0.7 mJy beam^{-1} (the rms noise). The 2.″5×3.″1 synthesized beam is indicated in the lower left of each panel. The bottom row compares the data (black points) and model (green line) in the visibility domain (left) as well as the SED (right). The model SED is the sum of three components: a Kurucz model photosphere (solid black line), a warm inner dust belt (dotted line), and a cold outer dust belt (dashed black line) that contributes effectively all the emission at millimeter wavelengths. The units of the ordinate are defined so that $L_\nu = 4\pi d^2 \nu F_\nu$ in units of $L_\odot$.

Tielens (2005), the dust temperature is given by

$$T_r = \left[\frac{L_*}{\sigma r^2} \frac{\pi^3}{240} \frac{1}{(\beta+3)!\zeta(\beta+4)Q_0} \left(\frac{\lambda_0 k}{hc}\right)^{-\beta} \right]^{\frac{1}{4+\beta}}, \quad (1)$$

where L_* is the stellar luminosity, σ is the Stefan-Boltzmann constant, r is the distance from the star, β is the dust grain emission efficiency power law index, ζ is the Riemann zeta function, and Q_0 is the dust grain efficiency at the critical wavelength $\lambda_0 = 2\pi a$. We assume a single characteristic grain size a, since this is sufficient to model the data and more complexity in the grain size distribution is not required to fit currently available data. The flux as a function of wavelength is then

$$F_\lambda = \frac{\pi a^2 Q(\lambda)}{d^2} \int_{r_{\rm in}}^{r_{\rm out}} 2\pi r\, B_\lambda(T_r)\, n(r)\, {\rm d}r, \quad (2)$$

where d is the distance to the source, $r_{\rm in}$ and $r_{\rm out}$ are the inner and outer radii of the dust disk, B_λ is the Planck function, and n is the number density of dust grains. The number density of grains is related to the surface mass density of dust grains as $\Sigma = n m_g$, where m_g is the mass per dust grain, and we parameterize Σ as a function of radius in the following way: $\Sigma(R) = \Sigma_{100}(100\,{\rm AU}/r)^p$. For consistency with previous works (e.g., Williams et al. 2004), we assume a standard millimeter-wavelength mass opacity of $1.8(\nu/10^{12}\,{\rm Hz})^{0.8}\,{\rm cm^2\,g^{-1}}$ (D'Alessio et al. 2001) evaluated at the 880 μm wavelength of the SMA data.

Because the outer dust belt is not bright enough at short wavelengths to reproduce the 24 and 33 μm *Spitzer* MIPS fluxes, we add a low-mass 69 K dust belt component to the SED (it would be entirely unresolved and contribute no detectable flux in the SMA data). The temperature is set to match that derived from the IR spectrum in Carpenter et al. (2009), and the mass is then varied to best reproduce the observed SED. We do not expect the properties of this belt to substantially affect the properties of the outer disk that is the focus of this analysis.

We also generate a model image assuming an inclination i=25° and position angle of the major axis PA=148° from the scattered light images (Ardila et al. 2004). We compare the spatially resolved model to the SMA observations in the visibility domain, using the MIRIAD task `uvmodel` to sample the model image at the same spatial frequencies as the SMA data after convolution with a 0.3" Gaussian seeing kernel.

To find the best-fit model parameters, we perform a χ^2 comparison between the model and the SED and SMA visibilities. We calculate a χ^2 value for the SED as a whole as well as for all of the real and imaginary visibilities at each spatial frequency and then simply sum the two values so that $\chi^2 = \chi^2_{\rm SED} + \chi^2_{\rm vis}$. As discussed in Andrews et al. (2009), due to a fortuitous balance between the quality and quantity of samples in the two data sets, each contributes roughly the same amount to the total χ^2 value, so that neither the SED nor the visi-

bility data dominates the final fit. We vary the dust grain properties $\{a,\beta\}$, the spatial parameters $\{r_{\rm in},r_{\rm out},p\}$, and the total mass in the disk $M_{\rm disk}$ and in the belt $M_{\rm belt}$. The total disk mass is related to the surface density as $M_{\rm disk} = 2\pi\Sigma_{100}(100\,AU)^p \frac{r_{\rm out}^{2-p} - r_{\rm in}^{2-p}}{2-p}$.

The six parameters effectively divide into two sets of three, with the spatial parameters $\{r_{\rm in},r_{\rm out},p\}$ allowing us to reproduce the morphology of the spatially resolved data and the dust parameters $\{a,\beta,M_{\rm disk}\}$ allowing us to match the SED. The characteristic grain size a affects the dust temperature and shifts the peak wavelength of the blackbody. β has a similar effect, but its influence on Q_λ is far more visible in determining the overall shape of the dust spectrum, particularly the slope with which the tail of the curve falls at long wavelengths. For the optically thin disk models we consider, the total mass $M_{\rm disk}$ acts as a normalizing factor, shifting the blackbody curve vertically to match the observed integrated millimeter flux. The visibilities are particularly sensitive to the inner radius $r_{\rm in}$, which is the dominant factor in determining the location of the first null in the visibility function, i.e., the shortest baseline at which the visibilities pass through zero and become negative. However, the narrower the ring, the greater the influence of the outer radius $r_{\rm out}$ on the null location, which can also be further moderated by how concentrated the emission is towards the inner radius, described by the surface density power law p. There is a fairly strong degeneracy between $r_{\rm out}$ and p; however, we include both parameters because the surface density power law is of interest for comparisons with the shorter-wavelength data.

We perform the χ^2 minimization in multiple steps, beginning with coarsely sampled grids and increasing the grid resolution to refine our estimates and avoid settling on a local rather than a global minimum. The initial coarse grid allows a to vary between 0.01 and 100 μm, β between -1 and 1.5, $M_{\rm disk}$ between 10^{-1} and 10^{-4} $M_\oplus$, $r_{\rm in}$ and $r_{\rm out}$ between 1 and 500 AU, and p from -1 to 4. Eventually the grids are refined so that the smallest (linear) steps are 1 μm for a, 0.1 for β, 10 AU for $r_{\rm in}$ and $r_{\rm out}$, 10^{-3} $M_\oplus$ for $M_{\rm disk}$, 0.1 for p, and 2×10^{-4} $M_\oplus$ for $M_{\rm belt}$. The uncertainties on each parameter are larger than the steps, although they are also frequently correlated with other parameters. Given the low signal-to-noise ratio of the data and the rapidly improving capabilities of millimeter interferometers, our intention is not to provide a detailed characterization of the disk and a robust statistical analysis of the errors, but rather to generate a representative model that can reproduce the gross features of the SED and visibilities (both SMA and CARMA, below) to constrain basic properties like the size, width, mass, and degree of axisymmetry of the dust ring.

The best-fit parameters are listed in Table 2. The debris belt is broad, extending from 50 to 170 AU. The negative surface density power law (p=-0.3) is unexpected, as circumstellar disk density is generally expected to decrease with distance from the star. The power law index is not tightly constrained, however (estimated uncorrelated uncertainty of $\pm$0.3), and with the relatively coarse spatial resolution, the SMA data could be smoothing over multiple belts of differing masses and radii. The masses of the two dust belts (0.41 $M_\oplus$ for the outer belt and 1.6×10^{-4} $M_\oplus$ for the inner belt) are fairly typical for multiple-belt debris systems. Figure 1 shows a comparison of the data and model in both the image and visibility domains, as well as for the SED. The images demonstrate that the model subtracts cleanly, leaving no difference at the $> 3\sigma$ level that would indicate an azimuthal asymmetry.

TABLE 2
Best-Fit Parameters for HD 107146

Parameter	Value
a (μm)	4
β	0.4
$r_{\rm in}$ (AU)	50
$r_{\rm out}$ (AU)	170
p	-0.3
$M_{\rm disk}$ ($M_\oplus$)	0.41
$M_{\rm belt}$ ($M_\oplus$)	1.6×10^{-4}

The best previous spatially resolved long-wavelength imaging of the HD 107146 disk is the 1.3 mm CARMA observation by Corder et al. (2009). As an *a posteriori* check on the robustness of our model, we predict the spatial distribution of flux at the CARMA frequency from our SED + SMA model, subtract the model in the visibility domain using the MIRIAD task uvmodel, and image the residuals. Figure 3 shows the results of this comparison: the SMA model prediction subtracts cleanly from the CARMA visibilities, leaving no residuals at the $> 3\sigma$ level. This also implies that an axisymmetric model is consistent with the millimeter-wavelength data obtained so far from the HD 107146 system.

4.2. *HR 8799 Modeling Procedure*

Because of the very low signal-to-noise ratio in the HR 8799 data, the full multiparameter treatment we apply to HD 107146 is not warranted. Instead, we (1) compare our data with the prediction of the SED-based model of Su et al. (2009), and (2) explore whether the data can discriminate between a narrow or broad dust ring around the star. Throughout the analysis, we assume that the disk is viewed face-on (i=0°). The inclination is likely closer to 20°, based on a range of diagnostics including rotational velocity $v \sin i$, astrometry of the planet orbits, stability analyses, and the marginally resolved *Spitzer* observations of an extended halo (Lafrenière et al. 2009; Reidemeister et al. 2009; Su et al. 2009; Fabrycky & Murray-Clay 2010; Moro-Martín et al. 2010). However, the data are not sensitive enough to distinguish between the two inclinations; neither are they sensitive enough to favor a particular position angle in any statistically meaningful way. As described below, it is difficult to determine the size of the disk from the visibilities alone to within a factor of two. The difference in radii derived for an inclination of 20° and 0° is only ∼7%, far less than the uncertainty in the data. Therefore, in the absence of a measurable position angle it is simplest to assume a face-on geometry.

Su et al. (2009) model three components to the dust distribution in the HR 8799 system: a warm (T∼150 K) inner dust belt, a cold (T∼45 K) outer planetesimal belt, and an extended (R∼300-1000 AU) halo of small grains. Since only the cold planetesimal belt contributes substantially to the flux at millimeter wavelengths, we compare our data to this component. The model has been revised to take into account the analysis of the system con-

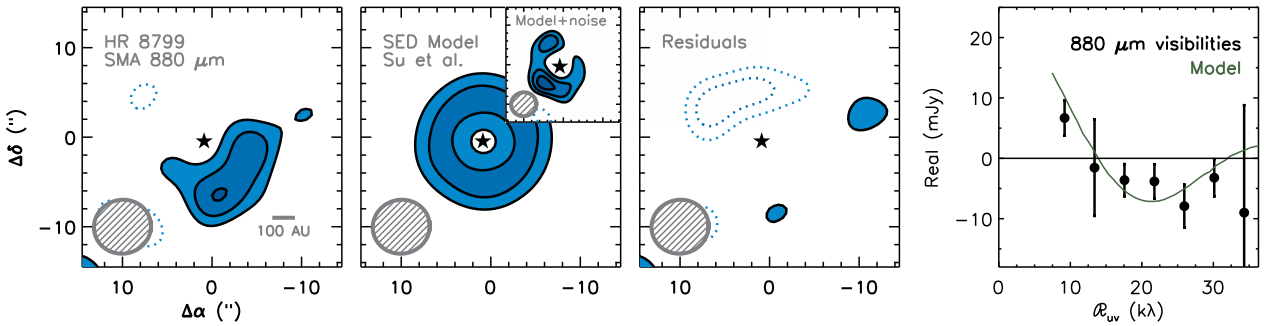

FIG. 2.— Comparison between HR 8799 millimeter data and the Su et al. (2009) model of the SED. The three image domain panels show the SMA 880 μm data (left), model (center), and residuals (right), with contours [2,3,4]×1.1 mJy beam^{-1} (the rms noise). The 6.″0×6.″4 synthesized beam is indicated in the lower left of each panel, and the inset in the center panel shows a model prediction with added noise at the level of the SMA data set. It should be noted that the arc of emission in the inset model with noise changes position depending on the particular noise in the simulation; the arc is a common feature of all models, but its position angle is not. The visibility domain plot to the right compares the data (black points) and the model (green line).

ducted by Moro-Martín et al. (2010). It includes a dust belt with constant surface density (but decreasing surface brightness) as a function of radius, with a sharp inner edge at a distance of 150 AU from the star and an outer edge at a radius of 300 AU. The location of the outer edge is consistent with constraints from single-dish observations: since the 870 μm flux is effectively identical in the 19" APEX beam (11.2±1.5 mJy; P. Kalas, priv. comm.) and the 14" JCMT beam (10.3±1.8 mJy Williams & Andrews 2006), the disk radius must be $\lesssim$300 AU. The total mass of the dust in the belt is 1.2×10^{-1} M$_\oplus$, with grains ranging in size from 8 μm to 1 mm.

The left panels of Figure 2 show an image-domain comparison between the SMA data and the SED-based model of Su et al. (2009), calculated at the same wavelength as the data. The inset in the central panel shows the predicted spatial distribution of emission for the Su et al. (2009) model observed with the same noise level as the SMA data; the 4σ peak offset by 6" from the star position and the partial arc of emission match well the observed morphology. The residuals subtract fairly cleanly, with only a slight negative 3σ peak. While such a large residual could potentially point to an azimuthal asymmetry in the dust distribution due to the gravitational influence of the planet HR 8799b, which is located at a similar azimuth to the negative peak, the signal-to-noise ratio is too low to permit a firm conclusion. The separation between the star and emission peak in the central panel inset is comparable to that in the data, certainly within the astrometric uncertainty of the observation. The right panel of Figure 2 makes the same comparison in the visibility domain, where the visibilities have been azimuthally averaged to enhance the signal-to-noise ratio in each bin. Within the uncertainties, the Su et al. (2009) model predicts well the spatially resolved data.

We also perform an exploration of the SMA visibilities and SED using a modified version of the method described in Section 4.1 aimed at determining whether the data can distinguish between a narrow or broad dust ring. To do so, we fix a to 1 μm, β to 0.5, and p to 0, implying a ring of constant surface density. We explore the narrow ring scenario by assuming that the width of the ring is 1 AU, and allowing only $r_{\rm in}$ to vary. The SED is assembled from the literature, including 2MASS, *IRAS*, and *Hipparcos* fluxes (Moshir 1989; Moór et al. 2006; Williams & Andrews 2006; Su et al. 2009). To reproduce the SED, we allow $M_{\rm disk}$ to vary, and add a 150 K belt of variable mass $M_{\rm belt}$, as in Su et al. (2009), to reproduce the observed mid-IR flux. We use a Kurucz-Lejune model photosphere (Lejeune et al. 1997) for a star of luminosity 4.92 L$_\odot$, radius 1.4 R$_\odot$, effective temperature 7250 K, and metallicity [Fe/H]=-0.5 (Sadakane 2006; Marois et al. 2008). The χ^2 minimization results in a best-fit model with a ring radius of 170 AU, with $M_{\rm disk}$ and $M_{\rm belt}$ equal to 5.5×10^{-4} and 4.0×10^{-6} M$_\oplus$, respectively.

The combination of SED and visibilities can help to distinguish between a narrow ring and a broad belt. The null in the visibility function of the SMA data occurs at roughly 12 kλ; using Equation A11 from Hughes et al. (2007), if the underlying flux distribution were a thin ring, it would have a radius of about 250 AU. On the other hand, if it were a broad ring like the Su et al. (2009) model predicts, then using Equation A9 of Hughes et al. (2007) the 12 kλ null implies a band with a smaller inner radius by up to a factor of 3, depending on how quickly the flux decreases with distance from the star. The 170 AU result for the ring obtained in our SED+visibility analysis is odd in this context, since it is roughly 2/3 the radius implied by the visibility null and the location of the emission peak. The mismatch is due to the SED fit: the ∼45 K temperature implied by the SED (Su et al. 2009) is warmer than would be predicted for a 250 AU ring given the assumed dust properties. The 170 AU result also depends strongly on the choice of a 1 μm dust grain size. If the grain size is allowed to vary, even smaller grain sizes are preferred, since raising the temperature of the dust grains results in a better match between the SED and visibilities. It is therefore difficult to reconcile the large radius of a thin ring implied by the visibility data with the relatively warm dust implied by the SED for a narrow ring configuration. Yet we have already shown that the observed flux distribution is also consistent with that predicted for a broad band of emission with an inner radius of ∼150 AU, as in the Su et al. (2009) model, which contains warmer dust than a narrow ring far from the star. This is consistent with the location of the visibility null for a broad ring configuration. Put another way, the spatially resolved SMA data *alone* are unable to discriminate between a narrow ring located

$\sim$200 AU from the star and a broad disk with an inner radius of $\sim$150 AU, but the *combination* of visibilities and SED favors the latter scenario. Spatially resolved data with a higher signal-to-noise ratio are required to place more stringent constraints on the dust morphology, although the spatially extended Su et al. (2009) model is capable of reproducing both the detailed SED properties and the SMA data.

5. DISCUSSION

The emerging theoretical framework for understanding debris disk structure postulates belts of planetesimals that produce a range of dust grain sizes through a collisional cascade (e.g. Wyatt 2008, and references therein). The "birth rings" in which dust is generated are typically assumed to be relatively radially narrow, and millimeter-size grains are predicted to be confined near the birth population while smaller grains are smeared to far larger distances through the effects of stellar radiation (e.g. Strubbe & Chiang 2006; Kuchner & Stark 2010). In this context, it is interesting to compare the morphology of the disks derived at millimeter wavelengths to the results of spatially resolved imaging at optical and infrared wavelengths.

The broad ring model derived for HD 107146 bears a striking similarity to the features of the scattered light observations of Ardila et al. (2004); Ertel et al. (2011). They infer the presence of a broad dust ring with peak optical depth at a distance of 130 AU from the star and FWHM 85 AU. The 880 μm SMA data have peak brightness at a distance of 5" ($\sim$115 AU) from the central star, with models of the spatially resolved data implying a broad ring extending from 50 to 170 AU, similar to the extent measured in the optical. The negative surface density power law of $p \sim -0.3$ implies a near-constant surface brightness with radius, similar to the two-power-law behavior (with optical depth increasing to a radius of 130 AU and decreasing beyond that radius) described for the scattered light. However, it is not at all obvious that the morphology of the 880 μm data *should* be so well matched to that of the F606W and F814W *HST* data, given the birth ring scenario and the prediction that the spatial extent of the small scatterers should exceed that of the millimeter-size particles. If enough molecular gas lingers in the system, it is possible that even the large dust grains could remain entrained in gas. It is also possible that the grain size distribution is concentrated at small sizes; multiwavelength imaging at higher signal-to-noise would be required to confirm this.

The HR 8799 disk is known to posess a large and surprisingly massive halo of small dust grains extending between $\sim$300-1000 AU from the star and resolved in 70 μm emission with *Spitzer* (Su et al. 2009). The mass of grains in the halo is about 15 times higher than expected for a static collisionally dominated disk (Wyatt et al. 2007), similar to the halo observed around Vega. This implies that the production of small grains is enhanced in these systems, most likely due to heavy dynamical stirring (Su et al. 2009). The broad ring of millimeter emission suggested by the SED model of Su et al. (2009) that is consistent with the 880 μm visibilities is likely to be generated by the same stirring process responsible for the enhanced production of small grains in the halo.

The other aspect of morphology worth mentioning is the degree of axisymmetry. There is no statistically significant evidence for deviations from axisymmetry in the disks that might point to dynamical resonances with a large planet. The 3σ negative residual in the HR 8799 observation coincides roughly with the position of the emission *peak* in the 350 μm CSO map presented in Patience et al. (2011), a likely indication that both features are in fact simply noise in the data. We do not confirm the azimuthal asymmetry suggested by CSO observations in Patience et al. (2011) despite higher resolution and signal-to-noise; within the (large) uncertainties the data are so far consistent with a symmetric disk. The inset in the center image panel of Fig. 2 illustrates how emission morphology in low signal-to-noise data sets may be misleading. We also note that the challenge of interpreting faint emission morphology from debris disk has lead to spurious detections of clumpy structure in the Vega (Koerner et al. 2001; Wilner et al. 2002; Piétu et al. 2011) and HD 107146 (Corder et al. 2009, this work) debris disks. Given these difficulties, greater sensitivity is necessary to point conclusively to a deviation from axisymmetry. Of course, the lack of deviations from axisymmetry does not necessarily imply a lack of giant planets; for example, Kuchner & Stark (2010) predict that the dynamical influence of Neptune should be invisible at millimeter wavelengths in our own solar system, and that the smoothing effect of collisions would be enhanced for larger optical depths comparable to the disks observed in this paper.

5.1. *Implications for Planetary Systems*

The location of the inner edge of the dust belt has profound implications for our understanding of the directly-imaged planetary system orbiting HR 8799. The visibilities alone constrain the inner radius of the dust belt to between 80 and 250 AU, while the combination of SED and visibilities favors an inner radius of approximately 150 AU. As discussed by Su et al. (2009), the 90 AU inner radius initially estimated from the SED is consistent with the estimated extent of the chaotic zone of HR 8799b. Assuming a semimajor axis equivalent to the projected separation of the planet from the star (68 AU) and the nominal planet mass of 5-11 M_J (Marois et al. 2008), the chaotic zone ranges from approximately 17 to 21 AU from the planet depending on the assumed stellar age. Assuming a nearly face-on circular orbit, this places the chaotic zone edge at a distance of $\sim$85 AU from the star. It is therefore conceivable that the inner edge of the debris belt is being shaped by the outermost planet if it does indeed fall near a radius of 90 AU. Simulations by Moro-Martín et al. (2010) make it clear that the planetary system parameters, for several of the dynamical configurations described in recent stability analyses (e.g., Fabrycky & Murray-Clay 2010; Goździewski & Migaszewski 2009), are consistent with an inner disk radius up to 150 AU in radius. This brings it into agreement with the larger radius implied by the combination of SMA and SED data. In fact, an exploration of the parameter space of stable planet masses and eccentricities reveals that a semimajor axis of 150 AU effectively serves as an upper limit to the radius at which the disk is plausibly truncated by the planetary chaotic zone for any planetary system configuration with long-term stability. Given the $\sim$20 M_J upper limit on the mass of the

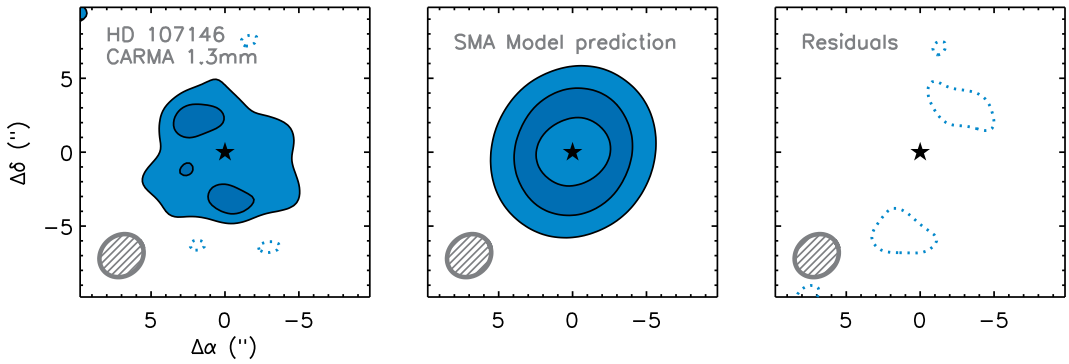

FIG. 3.— An *a posteriori* comparison between 1.3 mm CARMA observations of HD 107146 from Corder et al. (2009) and the model of disk structure based on the SED and 880 μm SMA visibilities. The three panels show the CARMA data as in Fig. 3 of Corder et al. (2009) (left), the model prediction at 1.3 mm derived from the SED and 880 μm SMA visibilities (center), and residuals (right). Contours are $[2,4]\times0.35$ mJy beam^{-1} (the rms noise), and the $3\farcs2\times2\farcs7$ synthesized beam is shown in the lower left of each panel. The disk structure model derived from the SED and 880 μm SMA visibilities agrees well with the spatial distribution of the 1.3 mm CARMA data, indicating that the emission arises from spatially coincident dust grain populations.

outermost planet (Fabrycky & Murray-Clay 2010), only configurations with the outermost planet in a marginally stable orbit with varying semimajor axis can extend the overlapping resonances of the chaotic zone out to such a large distance from the star. While a nonzero eccentricity of the outermost planet could also extend the radius of the dust belt, the dynamical stability criteria for the system generally allow only a planet at the lower end of the allowable mass range to achieve only a moderate eccentricity, ruling out the case of *both* a large mass and an eccentric orbit for HR 8799b. More sensitive observations that pinpoint the location of the inner edge of the dust belt more precisely will therefore provide important constraints on the long-term stability of the system. The similarity of the SED shape to that of Fomalhaut suggests that the inner edge of the disk is sharp (Su et al. 2009), which is also consistent with dynamical truncation by interactions with the planetary system. Knowing the geometry of the system would aid in determining whether or not the debris belt is truncated by HR 8799b, since the semimajor axis of both its orbit and the inner edge of the debris belt could be more precisely determined. If the belt is truncated by the outermost planet, this would also provide an independent dynamical estimate of the mass of the planet, which currently depends on the highly uncertain age of the system.

No companion has to date been observed in orbit around HD 107146. It seems clear that the inner edge of the debris ring is not sculpted by a stellar companion, as searches by Metchev & Hillenbrand (2009); Apai et al. (2008) have ruled out the presence of objects more massive than 10-12 M_J at separations of ∼15-75 AU from the star. However, there are no such limits on the presence of a $< 12\,M_J$ companion. Corder et al. (2009) discuss the features that a putative planet would possess if it were responsible for sculpting resonances in the debris disk; however, since the SMA observations and modeling presented here do not confirm the clumpy structure suggested by the CARMA data alone, the properties of a planet interacting with the debris would likely be somewhat different. Assuming that the inner edge of the debris belt corresponds with the outer edge of the planet's chaotic zone, a planet with mass between 1 and 10 M_J would most likely be located at a deprojected radial separation of ∼44 AU from the star, given the 50 AU inner radius derived from the SMA data.

Of course, there are physical mechanisms other than dynamical interactions with an embedded giant planet that are capable of generating the observed dust ring morphology. Despite the upper limit on the gas density in the disk, even after most of the original mass has dissipated remnant gas can aid in shaping broad rings and haloes in the dust (e.g., Takeuchi & Artymowicz 2001). The collisional cascade initiated by the formation of smaller planetesimals could also account for the set of broad bands implied by the observations of this system (e.g., Kenyon & Bromley 2004), and may be more consistent with the matching extent of the optical and millimeter emission. However, the timescale necessary to form large (∼1000 km) planetesimals at such a great distance from the star is only marginally consistent with the 160 Myr age of the system, and the width of the emission band is too large to arise from only one such ring of planet formation.

6. SUMMARY AND CONCLUSIONS

We have obtained the first spatially resolved 880 μm observations of the dusty debris disks around the young solar analogue HD 107146 and the multiple-planet host star HR 8799 at a resolution of 3" and 6", respectively. The data reveal broad bands of emission with inner radii at tens of AU from the central star. Models of axisymmetric dust annuli are capable of reproducing both the SED and 880 μm visibility data, with no significant residuals that would indicate clumpiness due to shepherding of dust grains into orbital resonances with planets. The outer debris belt around HR 8799 is spatially resolved for the first time. While the spatially resolved data alone are not of sufficiently sensitive to constrain the location of the inner edge of the HR 8799 disk, the SED-based model of Su et al. (2009) with an inner edge at 150 AU from the star is shown to be consistent with the SMA data. A 150 AU inner radius serves roughly as the largest radius at which the debris belt may be plausibly truncated by the chaotic zone of HR 8799b, and more sensitive imaging better able to pinpoint the location of the inner edge of the debris belt would be extremely valuable. The 880 μm observations of HD 107146 are con-

sistent with previous spatially resolved disk observations at 1.3 mm (Corder et al. 2009) and in the near-infrared (Ardila et al. 2004), although we demonstrate that the long-wavelength data are distributed smoothly to within the precision of the observations. For both systems, there is some indication that the population of dust grains giving rise to the millimeter data are located closer to the star than the likely smaller populations probed by the short-wavelength data, consistent with theoretical predictions for collisional destruction leading to blow-out of small dust.

Long-wavelength observations with higher sensitivity will be particularly exciting for the case of HR 8799, since they will be able to constrain the disk geometry (inclination and position angle) and more precisely determine the location of the inner edge of the dust belt, both of which will place important dynamical constraints on the masses of the directly-imaged planets in the system.

The authors are grateful to Stuartt Corder and John Carpenter for sharing their HD 107146 CARMA data. We also thank Eugene Chiang for constructive comments on the paper. A. M. H. is supported by a fellowship from the Miller Institute for Basic Research in Science.

REFERENCES

Andrews, S. M., Wilner, D. J., Hughes, A. M., Qi, C., & Dullemond, C. P. 2009, ApJ, 700, 1502
Apai, D., Janson, M., Moro-Martín, A., Meyer, M. R., Mamajek, E. E., Masciadri, E., Henning, T., Pascucci, I., Kim, J. S., Hillenbrand, L. A., Kasper, M., & Biller, B. 2008, ApJ, 672, 1196
Ardila, D. R., Golimowski, D. A., Krist, J. E., Clampin, M., Williams, J. P., Blakeslee, J. P., Ford, H. C., Hartig, G. F., & Illingworth, G. D. 2004, ApJ, 617, L147
Bryden, G., Beichman, C. A., Trilling, D. E., Rieke, G. H., Holmes, E. K., Lawler, S. M., Stapelfeldt, K. R., Werner, M. W., Gautier, T. N., Blaylock, M., Gordon, K. D., Stansberry, J. A., & Su, K. Y. L. 2006, ApJ, 636, 1098
Carpenter, J. M., Bouwman, J., Mamajek, E. E., Meyer, M. R., Hillenbrand, L. A., Backman, D. E., Henning, T., Hines, D. C., Hollenbach, D., Kim, J. S., Moro-Martin, A., Pascucci, I., Silverstone, M. D., Stauffer, J. R., & Wolf, S. 2009, ApJS, 181, 197
Carpenter, J. M., Bouwman, J., Silverstone, M. D., Kim, J. S., Stauffer, J., Cohen, M., Hines, D. C., Meyer, M. R., & Crockett, N. 2008, ApJS, 179, 423
Carpenter, J. M., Wolf, S., Schreyer, K., Launhardt, R., & Henning, T. 2005, AJ, 129, 1049
Chen, C. H., Sheehan, P., Watson, D. M., Manoj, P., & Najita, J. R. 2009, ApJ, 701, 1367
Chiang, E., Kite, E., Kalas, P., Graham, J. R., & Clampin, M. 2009, ApJ, 693, 734
Corder, S., Carpenter, J. M., Sargent, A. I., Zauderer, B. A., Wright, M. C. H., White, S. M., Woody, D. P., Teuben, P., Scott, S. L., Pound, M. W., Plambeck, R. L., Lamb, J. W., Koda, J., Hodges, M., Hawkins, D., & Bock, D. 2009, ApJ, 690, L65
Currie, T., Burrows, A., Itoh, Y., Matsumura, S., Fukagawa, M., Apai, D., Madhusudhan, N., Hinz, P. M., Rodigas, T. J., Kasper, M., Pyo, T.-S., & Ogino, S. 2011, ApJ, 729, 128
D'Alessio, P., Calvet, N., & Hartmann, L. 2001, ApJ, 553, 321
Ertel, S., Wolf, S., Metchev, S., Schneider, G., Carpenter, J. M., Meyer, M. R., Hillenbrand, L. A., & Silverstone, M. D. 2011, ArXiv e-prints
Fabrycky, D. C. & Murray-Clay, R. A. 2010, ApJ, 710, 1408
Goździewski, K. & Migaszewski, C. 2009, MNRAS, 397, L16
Gray, R. O. & Kaye, A. B. 1999, AJ, 118, 2993
Habing, H. J., Dominik, C., Jourdain de Muizon, M., Laureijs, R. J., Kessler, M. F., Leech, K., Metcalfe, L., Salama, A., Siebenmorgen, R., Trams, N., & Bouchet, P. 2001, A&A, 365, 545
Hillenbrand, L. A., Carpenter, J. M., Kim, J. S., Meyer, M. R., Backman, D. E., Moro-Martín, A., Hollenbach, D. J., Hines, D. C., Pascucci, I., & Bouwman, J. 2008, ApJ, 677, 630
Hinz, P. M., Rodigas, T. J., Kenworthy, M. A., Sivanandam, S., Heinze, A. N., Mamajek, E. E., & Meyer, M. R. 2010, ApJ, 716, 417
Hughes, A. M., Wilner, D. J., Calvet, N., D'Alessio, P., Claussen, M. J., & Hogerheijde, M. R. 2007, ApJ, 664, 536
Jaschek, M. 1978, Bulletin d'Information du Centre de Donnees Stellaires, 15, 121
Kenyon, S. J. & Bromley, B. C. 2004, AJ, 127, 513
Koerner, D. W., Sargent, A. I., & Ostroff, N. A. 2001, ApJ, 560, L181
Kuchner, M. J. & Stark, C. C. 2010, AJ, 140, 1007
Lafrenière, D., Marois, C., Doyon, R., & Barman, T. 2009, ApJ, 694, L148
Landolt, A. U. 1983, AJ, 88, 853
Lejeune, T., Cuisinier, F., & Buser, R. 1997, A&AS, 125, 229
Maness, H. L., Fitzgerald, M. P., Paladini, R., Kalas, P., Duchene, G., & Graham, J. R. 2008, ApJ, 686, L25
Marois, C., Macintosh, B., Barman, T., Zuckerman, B., Song, I., Patience, J., Lafrenière, D., & Doyon, R. 2008, Science, 322, 1348
Marois, C., Zuckerman, B., Konopacky, Q. M., Macintosh, B., & Barman, T. 2010, Nature, 468, 1080
Matthews et al. submitted
Metchev, S. A. & Hillenbrand, L. A. 2009, ApJS, 181, 62
Moór, A., Ábrahám, P., Derekas, A., Kiss, C., Kiss, L. L., Apai, D., Grady, C., & Henning, T. 2006, ApJ, 644, 525
Moór, A., Pascucci, I., Kóspál, Á., Ábrahám, P., Csengeri, T., Kiss, L. L., Apai, D., Grady, C., Henning, T., Kiss, C., Bayliss, D., Juhász, A., Kovács, J., & Szalai, T. 2010, ArXiv e-prints
Moro-Martín, A., Malhotra, R., Bryden, G., Rieke, G. H., Su, K. Y. L., Beichman, C. A., & Lawler, S. M. 2010, ApJ, 717, 1123
Moshir, M. 1989, IRAS Faint Source Survey, Explanatory supplement version 1 and tape, ed. Moshir, M.
Moya, A., Amado, P. J., Barrado, D., García Hernández, A., Aberasturi, M., Montesinos, B., & Aceituno, F. 2010, MNRAS, 405, L81
Najita, J. & Williams, J. P. 2005, ApJ, 635, 625
Owen, F. N., Hardee, P. E., & Bignell, R. C. 1980, ApJ, 239, L11
Patience, J., Bulger, J., King, R. R., Ayliffe, B., Bate, M. R., Song, I., Pinte, C., Koda, J., Dowell, C. D., & Kovacs, A. 2011, ArXiv e-prints
Perryman, M. A. C., Lindegren, L., Kovalevsky, J., Hoeg, E., Bastian, U., Bernacca, P. L., Crézé, M., Donati, F., Grenon, M., van Leeuwen, F., van der Marel, H., Mignard, F., Murray, C. A., Le Poole, R. S., Schrijver, H., Turon, C., Arenou, F., Froeschlé, M., & Petersen, C. S. 1997, A&A, 323, L49
Piétu, V., Di Folco, E., Guilloteau, S., Gueth, F., & Cox, P. 2011, ArXiv e-prints
Reidemeister, M., Krivov, A. V., Schmidt, T. O. B., Fiedler, S., Müller, S., Löhne, T., & Neuhäuser, R. 2009, A&A, 503, 247
Sadakane, K. 2006, PASJ, 58, 1023
Sadakane, K. & Nishida, M. 1986, PASP, 98, 685
Silverstone, M. D. 2000, PhD thesis, UNIVERSITY OF CALIFORNIA, LOS ANGELES
Strubbe, L. E. & Chiang, E. I. 2006, ApJ, 648, 652
Su, K. Y. L., Rieke, G. H., Stapelfeldt, K. R., Malhotra, R., Bryden, G., Smith, P. S., Misselt, K. A., Moro-Martin, A., & Williams, J. P. 2009, ApJ, 705, 314
Takeuchi, T. & Artymowicz, P. 2001, ApJ, 557, 990
Tielens, A. G. G. M. 2005, The Physics and Chemistry of the Interstellar Medium, ed. Tielens, A. G. G. M.
Williams, J. P. & Andrews, S. M. 2006, ApJ, 653, 1480
Williams, J. P., Najita, J., Liu, M. C., Bottinelli, S., Carpenter, J. M., Hillenbrand, L. A., Meyer, M. R., & Soderblom, D. R. 2004, ApJ, 604, 414

Wilner, D. J., Andrews, S. M., & Hughes, A. M. 2010, ArXiv e-prints
Wilner, D. J., Holman, M. J., Kuchner, M. J., & Ho, P. T. P. 2002, ApJ, 569, L115
Wyatt, M. C. 2006, ApJ, 639, 1153
—. 2008, ARA&A, 46, 339
Wyatt, M. C., Smith, R., Su, K. Y. L., Rieke, G. H., Greaves, J. S., Beichman, C. A., & Bryden, G. 2007, ApJ, 663, 365